

Moiré Dirac fermions in transition metal dichalcogenides heterobilayers

Chenglong Che(车成龙), Yawei Lv(吕亚威), and Qingjun Tong(童庆军)
Citation: Chin. Phys. B, 2023, 32 (**10**): 107307. DOI: 10.1088/1674-1056/aceee5
Journal homepage: http://cpb.iphy.ac.cn; http://iopscience.iop.org/cpb

What follows is a list of articles you may be interested in

Perspectives of spin-valley locking devices

Lingling Tao(陶玲玲)
Chin. Phys. B, 2023, 32 (**10**): 107306. DOI: 10.1088/1674-1056/acc809

Single-layer intrinsic 2H-phase LuX_2 (X = Cl, Br, I) with large valley polarization and anomalous valley Hall effect

Chun-Sheng Hu(胡春生), Yun-Jing Wu(仵允京), Yuan-Shuo Liu(刘元硕), Shuai Fu(傅帅),Xiao-Ning Cui(崔晓宁), Yi-Hao Wang(王易昊), and Chang-Wen Zhang(张昌文)
Chin. Phys. B, 2023, 32 (**3**): 037306. DOI: 10.1088/1674-1056/ac89d6

Recent advances of defect-induced spin and valley polarized states in graphene

Yu Zhang(张钰), Liangguang Jia(贾亮广), Yaoyao Chen(陈瑶瑶), Lin He(何林), and Yeliang Wang(王业亮)
Chin. Phys. B, 2022, 31 (**8**): 087301. DOI: 10.1088/1674-1056/ac70c4

alley-dependent transport in strain engineering graphene heterojunctions

Fei Wan(万飞), X R Wang(王新茹), L H Liao(廖烈鸿), J Y Zhang(张嘉颜),M N Chen(陈梦南), G H Zhou(周光辉), Z B Siu(萧卓彬), Mansoor B. A. Jalil, and Yuan Li(李源)
Chin. Phys. B, 2022, 31 (**7**): 077302. DOI: 10.1088/1674-1056/ac5613

Improvement of valley splitting and valley injection efficiency for graphene/ferromagnet heterostructure

Longxiang Xu(徐龙翔), Wengang Lu(吕文刚), Chen Hu(胡晨), Qixun Guo(郭奇勋), Shuai Shang(尚帅), Xiulan Xu(徐秀兰), Guanghua Yu(于广华), Yu Yan(岩雨), Lihua Wang(王立华), Jiao Teng(滕蛟)
Chin. Phys. B, 2020, 29 (**7**): 077304. DOI: 10.1088/1674-1056/ab8db2

SPECIAL TOPIC — Valleytronics

Moiré Dirac fermions in transition metal dichalcogenides heterobilayers

Chenglong Che(车成龙), Yawei Lv(吕亚威)[†], and Qingjun Tong(童庆军)[‡]

School of Physics and Electronics, Hunan University, Changsha 410082, *China*

(Received 31 May 2023; revised manuscript received 24 July 2023; accepted manuscript online 10 August 2023)

Monolayer group-VIB transition metal dichalcogenides (TMDs) feature low-energy massive Dirac fermions, which have valley contrasting Berry curvature. This nontrivial local band topology gives rise to valley Hall transport and optical selection rules for interband transitions that open up new possibilities for valleytronics. However, the large bandgap in TMDs results in relatively small Berry curvature, leading to weak valley contrasting physics in practical experiments. Here, we show that Dirac fermions with tunable large Berry curvature can be engineered in moiré superlattice of TMD heterobilayers. These moiré Dirac fermions are created in a magnified honeycomb lattice with its sublattice degree of freedom formed by two local moiré potential minima. We show that applying an on-site potential can tune the moiré flat bands into helical ones. In short-period moiré superlattice, we find that the two moiré valleys become asymmetric, which results in a net spin Hall current. More interestingly, a circularly polarized light drives these moiré Dirac fermions into quantum anomalous Hall phase with chiral edge states. Our results open a new possibility to design the moiré-scale spin and valley physics using TMD moiré structures.

Keywords: moiré superlattice, valleytronics, transition metal dichalcogenide, quantum anomalous Hall state

PACS: 73.90.+f, 68.65.Cd, 68.65.–k, 05.30.Rt **DOI:** 10.1088/1674-1056/aceee5

1. Introduction

Many two-dimensional (2D) materials have degenerate energy extrema located at inequivalent momentum points in the Brillouin zone, which introduces the valley degree of freedom for quasiparticles.[1,2] This valley index can be used to encode information, forming the basis of valleytronics.[3,4] Because different valleys are separated from each other in the momentum space, the scattering between them is largely suppressed. A prerequisite for the realization of this tempting idea is to manipulate the valley degree of freedom.[5]

The breaking of inversion symmetry has been recognized to be crucial to distinguish and further manipulate the valley degree of freedom.[6] It has been shown that, in Dirac materials without inversion symmetry, there exist valley contrasting Berry curvature and orbital magnetic moment, which result in valley dependent Hall transport and optical selection rules for interband transitions.[7–9] The latter effect means that a circularly polarized light can selectively pump the two valleys, suggesting an optical way to realize valley polarization. Following these theoretical predictions, subsequent experiments have successfully generated valley polarization in monolayer TMDs, which break intrinsically the inversion symmetry in their monolayer limit.[10–12] Besides valley polarization, valley current is another requirement to function the valleytronic devices. Several experimental activities have been taken in TMD materials based on the valley Hall effect.[13–15] However, because of the large intrinsic band gap in TMDs, the Berry curvature is relatively small, which makes the generated valley contrasting physics not robust in practical experiments. We also notice that the quantum valley Hall state and valley polarization quantum anomalous Hall state in-principle can provide topologically protected valley current, however, the realization of which needs carefully engineered spin–orbital coupling (SOC) and applied external magnetic field.

Stacking different 2D materials to form van der Waals (vdW) heterostructures offers exciting opportunities for studying low-dimensional physics and functional devices.[16] A general feature of vdW heterostructures is the formation of a long-range quasi-periodic structure, i.e., moiré pattern, due to the lattice mismatch and twist between the constituent layers.[17–20] For a long-wavelength moiré pattern, within a length scale much larger than the lattice constant but small compared to the moiré period, the atomic registry has negligible difference from commensurate bilayers, while varies smoothly over long range.[21] This unique atomic superlattice offers new opportunity to explore novel quantum phases in the 2D limit, such as topological insulator superlattice,[21] moiré skyrmions,[22] moiré excitons[23–27] and strongly correlated electronic states.[28–33] These novel quantum phases have opened up a new avenue for studying valleytronics.

In this paper, we show that Dirac fermions with tunable large Berry curvatures can be realized in the moiré pattern formed by the TMD heterobilayers. In particular, our first-

[†]Corresponding author. E-mail: lvyawei@hnu.edu.cn
[‡]Corresponding author. E-mail: tongqj@hnu.edu.cn

© 2023 Chinese Physical Society and IOP Publishing Ltd

principles results show that the moiré potential has two nearly degenerate extrema, which resembles a magnified gapped graphene lattice and gives rise to valley-indexed moiré Dirac fermions. Applying on-site potential on the two outmost zigzag edges of the moiré lattice, we can tune the gapped flat-band edge states into gapless helical ones. In addition, we find that in short-period moiré lattice, the two moiré valleys become asymmetric due to the triangular wrapping effect, which can give rise to a net spin Hall current in the presence of an in-plane electric field. Interestingly, applying a circularly polarized light can drive the moiré system into quantum anomalous Hall phase with topological chiral edge states. Our result provides an interesting possibility to explore the moiré-scale spin and valley physics in vdW heterostructures.

2. Valley contrasting physics in massive Dirac model

Before discussing the moiré Dirac fermions in TMDs heterobilayer, we first review briefly the valley contrasting physics in massive Dirac model that describes the low-energy physics of monolayer TMDs. TMDs have chemical formula MX_2, where M is a transition metal element (Mo or W) and X is a chalcogenide element (S, Se or Te). Similar to graphite, bulk TMDs are indirect bandgap semiconductors, and formed by stacking different layers together by weak vdW force. Within each layer, the metal atoms are coordinated by three adjacent chalcogenide elements in a triangular prism geometry, together forming a 2D honeycomb lattice from a top view. Unlike bulk TMDs, monolayer TMDs have direct bandgap located at the $\pm K$ points in the first Brillouin zone, giving the valley degree of freedom.[3,4] We notice that the inversion symmetry is intrinsically broken for monolayer TMDs. Arising from the d orbital nature, a strong SOC of several hundred meV is found in the valence band, resulting in spin–valley locked physics.[9]

The low-energy physics of monolayer TMDs can be effectively described by a massive Dirac Hamiltonian[9]

$$H = at(\tau k_x \sigma_x + k_y \sigma_y) + \frac{M}{2}\sigma_z - \lambda\tau\frac{\sigma_z - 1}{2}s_z, \tag{1}$$

where σ is the Pauli matrix for the basis functions consisting of Bloch states at $\pm K$ points, a is the lattice constant, t is the effective hopping integral, $\tau = \pm 1$ is the valley index, M is the Dirac mass (energy gap at $\pm K$ points), and s_z is the Pauli matrix for spin. In this model, the spin-up ($\uparrow$) and spin-down ($\downarrow$) components are completely decoupled and s_z remains a good quantum number. Figure 1(a) shows the energy spectrum of monolayer MoS_2 around the two valleys, which has a large SOC-induced splitting of 2λ at the valence bands. The Dirac model has nontrivial local band topology, which is characterized by the Berry curvature. In a 2D material, it is defined as $\Omega_n(\boldsymbol{k}) = \hat{z}\cdot\nabla_{\boldsymbol{k}}\times\langle u_n(\boldsymbol{k})|\mathrm{i}\nabla_{\boldsymbol{k}}|u_n(\boldsymbol{k})\rangle$, with n being the band index. From Eq. (1), the Berry curvature for the conduction band is

$$\Omega_c(\boldsymbol{k}) = -\tau\frac{2a^2t^2M'}{[M'^2 + 4a^2t^2k^2]^{3/2}}, \tag{2}$$

where $M' = M - \tau s_z\lambda$. The distribution of the Berry curvature in momentum space is shown in Fig. 1(b). As required by time reversal symmetry, the Berry curvatures from K valley and $-K$ valley have the same amplitudes but opposite signs, which gives rise to valley contrasting transverse electric current in the presence of an in-plane longitudinal electric field.

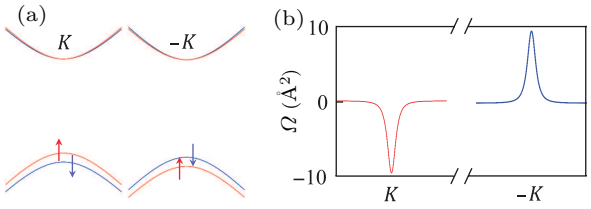


Fig. 1. (a) Schematic diagram of energy bands around the two valleys. The valley and spin indexes are indicated. (b) Distribution of Berry curvature $\Omega(\boldsymbol{k})$ around the two valleys in the conduction band of monolayer MoS_2, given in units of Å^2. The parameters used are $a = 3.193$ Å, $t = 1.10$ eV, $\lambda = 0.075$ eV and $M = 1.66$ eV.

First-principles results show that the Bloch states of monolayer TMDs near the band edges are mainly contributed by d_{z^2}, d_{xy}, and $d_{x^2-y^2}$ orbitals of metal atoms.[34] To facilitate the band structure calculation, a tight-binding (TB) model is constructed using these three orbitals, with parameters fitted according to the first-principles results. The TB model that only considers the nearest neighbor hopping between metal atoms can well reproduce the band structures near the $\pm K$ points, where we mainly focus in this work.

The three-band TB Hamiltonian reads

$$H_T = \sum_{i=1}^{N}\sum_{m}\varepsilon_m c_{im}^{\dagger}c_{im} + \sum_{\langle i,j\rangle}\sum_{m,n}t_{im,jn}c_{im}^{\dagger}c_{jn}, \tag{3}$$

where $\{m,n\} = \{d_{z^2}, d_{xy}, d_{x^2-y^2}\}$ are the orbital indices and $t_{im,jn}$ is the hopping integral between different orbitals and ε_m is the on-site energy. The SOC can be incorporated by $H_{\mathrm{SOC}} = \lambda\boldsymbol{L}\cdot\boldsymbol{S}$. The details of parameters for various TMDs are given explicitly in reference.[34]

3. Moiré Dirac fermions

Form Eq. (2), one can see that the magnitude of the Berry curvature is inversely proportional to the bandgap of the Dirac materials. In the following, we discuss the possibility of using moiré potential to engineer Dirac fermions with tunable small bandgap.

3.1. Moiré potential in TMDs heterobilayers

Because of the large number of atoms involved ($\propto (L/a)^2$), a direct first-principles calculation of the electronic property of a moiré pattern is challenging [c.f. Fig. 2(a)].

However, in a long-period moiré pattern, each local registry resembles lattice matched commensurate structure, one can first study electronic property at each local region and then map to the whole moiré pattern using a local approximation. In a semiconductor heterobilayer, the band-edge state is mainly contributed from one layer. The influence from the other layer can be taken into account by defining a moiré potential $V(\boldsymbol{r})$, which depends on the interlayer atomic registry $\boldsymbol{r}$. Because the interlayer distance is typically much larger than the in-plane variation in a unit cell, one can approximate $V(\boldsymbol{r})$ by a Fourier expansion that includes only the six moiré reciprocal lattice vectors in the first shell,[35]

$$V(\boldsymbol{r}) = \nu \sum_i \exp(\boldsymbol{b}_i \cdot \boldsymbol{r} + \varphi) + V_0, \tag{4}$$

where the summation over $\boldsymbol{b}_i$ is restricted to the six moiré reciprocal lattice vectors as shown in Fig. 2(c). Because the potential is real and each TMDs monolayer has threefold-rotation symmetry, we have $\nu(\hat{R}_{2\pi/3}\boldsymbol{b}) = \nu(\boldsymbol{b})$ and $\nu(\boldsymbol{b}) = \nu^*(-\boldsymbol{b})$. The three parameters $\{\nu, \varphi, V_0\}$ can be obtained by fitting from first-principles results at the three high-symmetry lattice-matched configurations [c.f. Fig. 2(b)].

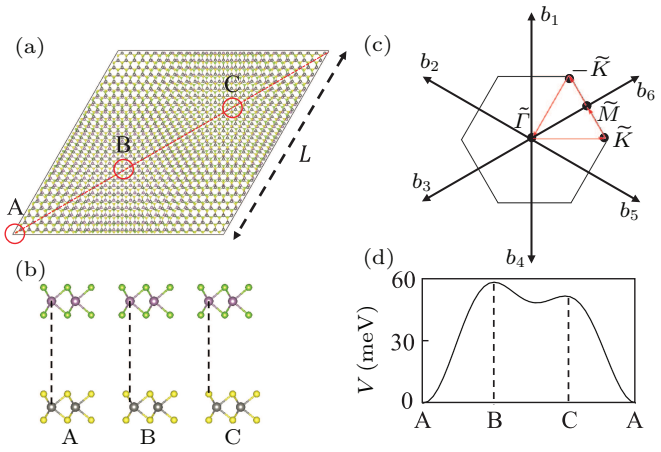


Fig. 2. (a) Schematic diagram of a moiré pattern formed in TMDs heterostructures. The three high-symmetry locals are labeled. L is the moiré periodicity. (b) Magnified view of three high-symmetry stacking configurations. A, B, and C stand for configurations with a metal atom of the top layer sitting right on top of a metal atom, hollow center, and chalcogen atom of the bottom layer, respectively. Purple and gray balls represent transition metal atoms, green and yellow balls represent chalcogenide atoms. (c) The six reciprocal lattice vectors of the moiré pattern with $|\boldsymbol{b}| = \frac{4\pi}{\sqrt{3}L}$. The hexagon gives the first moiré Brillouin zone. (d) Moiré potential for the valence band of a $MoSe_2/WS_2$ heterobilayer along the long diagonal of the moiré supercell, featuring two local maxima.

The first-principles calculations are performed with the open-source QUANTUM ESPRESSO plane-wave density functional theory (DFT) package.[36,37] The Perdew–Burke–Ernzerhof (PBE) exchange–correlation functional with semi-empirical DFT-D3 vdW correction method is adopted.[38] The plane-wave cut-off energy is set to 1115 eV. The crystal structures are fully relaxed until the force on each atom and total energy variations are smaller than 2.6×10^{-3} eV/Å and 1.4×10^{-4} eV. To avoid mirror interactions in the thickness direction, a vacuum space of 15 Å is used between adjacent heterostructures. The Brillouin zone k-point samplings are $10 \times 10 \times 1$ for both crystal optimizations and electronic structure computations. The obtained band-edge energy of the R-type $MoSe_2/WS_2$ heterobilayer for different configurations (as referenced by a common vacuum level) is listed in Table 1, from which the parameters $\{\nu, \varphi, V_0\} = \{-6.4\ \text{meV}, 234°, 38.3\ \text{meV}\}$ defined in the moiré potential of Eq. (4) can be extracted. We find that the moiré potential has two local maxima for holes located at WS_2 layer, with an energy difference of about 7 meV [c.f. Fig. 2(d)] and forming a honeycomb lattice. Furthermore, we have checked that for the H-type $MoSe_2/WS_2$ heterobilayer, the moiré potential forms a triangular lattice for holes located at WS_2 layer.

Table 1. First-principles calculated band-edge energy for the three high-symmetry configurations of the R-type $MoSe_2/WS_2$ heterobilayer [see Fig. 2(b)]. Energy is given in units of eV.

	A	B	C
$MoSe_2/WS_2$	−5.211	−5.204	−5.265

3.2. Moiré Dirac fermions in TMDs heterobilayers

Although the moiré potential breaks the original translation symmetry of each monolayer, the appearance of moiré periodicity in the heterostructure guarantees the application of Bloch theory and results in the formation of moiré minibands. We mainly focus on the electronic property of the heterostructure around the valence band, which can be modeled by adding directly a moiré potential $V(\boldsymbol{R})$ on the TB Hamiltonian of monolayer TMDs. We assume that the moiré pattern is formed between two rigid lattices, where the mapping between the local registry $\boldsymbol{r}$ and location $\boldsymbol{R}$ is linear. Therefore, the $\boldsymbol{r}$ dependence of the interlayer potential in commensurate bilayers can be directly mapped to the location $(\boldsymbol{R})$ dependence of the interlayer potential in a moiré. Under this approximation, the moiré modulated interlayer potential as a function of $\boldsymbol{R}$ is isomorphic to $V(\boldsymbol{r})$, i.e., $V(\boldsymbol{R}) \equiv V(\boldsymbol{r}(R))$.[21,35] In terms of this moiré potential, the TB Hamiltonian of the TMD heterostructure reads

$$\hat{H} = \sum_{i=1}^{N} \sum_m [\varepsilon_m + V(\boldsymbol{R}_i)] c_{im}^\dagger c_{im} + \sum_{\langle i,j \rangle} \sum_{m,n} t_{im,jn} c_{im}^\dagger c_{jn}, \tag{5}$$

the SOC can also be included in the calculation. We note that because the coupling between the two layers can be modulated by applying external vertical electric field and pressure, the moiré potential is experimentally tunable. A similar procedure has been introduced for excitons in TMD heterobilayer,[23,24] in which localized excitons have been experimentally observed.[25–27]

For moiré potential with only one energy minimum, a triangular lattice is formed, which has been proposed to study Hubbard model physics.[35,39] For moiré potential with two

nearly degenerate extrema, a hexagonal lattice is formed, which allows for the creation of moiré Dirac fermions with additional moiré valley degree of freedom appearing in the minibands. For an R-type $MoSe_2/WS_2$ heterobilayer, our first-principles results show that the moiré potential has two local maxima for holes mainly contributed from WS_2 layer, with an energy difference of about 7 meV [c.f. Fig. 2(d)]. Figure 3(a) shows the moiré miniband around the valence band edge, which features two gapped Dirac cones. The two cones locate at in-equivalent $\pm\widetilde{K}$ corners of the mini-Brillouin zone, defining a moiré valley degree of freedom. The miniband structure can be understood from the intra and inter moiré hopping of the localized state at each confinement center and well fitted by a TB Hamiltonian including only the nearest-neighbor hopping on a hexagonal lattice in the moiré scale

$$H_D = \sum_i \varepsilon_i a_i^\dagger a_i + t_0 \sum_i a_i^\dagger a_{i+1} + \text{h.c.}, \tag{6}$$

where t_0 is the hopping integral and $\varepsilon_i = \pm\Delta/2$ is the on-site energy for the two sublattices. The fitted hopping parameter t_0 (purple line with triangles) and Δ (black line with disks) as a function of moiré periodicity L are shown in Fig. 3(c). The moiré hexagonal lattice resembles a magnified graphene, which enables fine tuning on each moiré site. Applying opposite potentials on the two outmost zigzag edges of a moiré lattice tunes the gapped flat-band edge states into gapless helical ones [c.f. Fig. 3(d)].[40] These in-gap edge states are well separated from the bulk ones and propagate with opposite velocities and moiré valley indexes, thus opening up a new possibility to manipulate 1D topological state in the moiré scale.

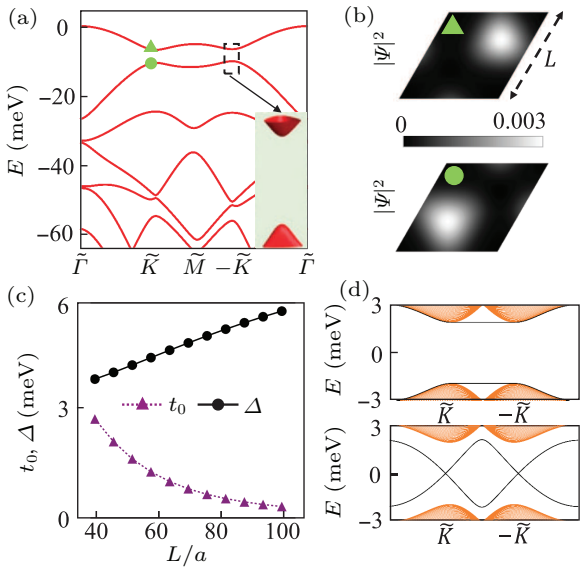


Fig. 3. (a) Minibands with moiré Dirac cones for an R-type $MoSe_2/WS_2$ heterobilayer with $L = 42a$, a being the lattice constant of WS_2. Inset: full dispersion near the moiré Dirac point $-\widetilde{K}$. (b) Wavefunction distribution at moiré Dirac point $\widetilde{K}$ indicated by the green triangle and dot in (a). (c) Fitted parameters t_0 and Δ in Eq. (6) as a function of moiré periodicity L. (d) The edge states of a moiré ribbon can be tuned from flat (upper plot) to helical (lower plot) by adding an on-site potential of $1.7t_0$ and $-1.7t_0$ at the two outmost zigzag edges. The parameters used are $t_0 = 2.37$ meV, $\Delta = 3.845$ meV.

Hexagonal lattice with a staggered sublattice potential has been widely explored to study Berry phase supported topological transport.[41–43] The Berry curvature, which leads to an anomalous velocity in the transverse direction in the presence of an in-plane electric field, at the moiré Dirac point $\pm\widetilde{K}$ in the conduction band is $\Omega(\widetilde{\tau}\widetilde{K}) = -2\widetilde{\tau}L^2t_0^2/\Delta^2$, where $\widetilde{\tau}$ is the moiré valley index. Compared with Dirac fermions in monolayer semiconductor, Berry curvature in moiré Dirac fermions is magnified by a factor $\propto (L/a)^2$. This giant Berry curvature leads to a large moiré valley Hall current, which can be detected as a giant nonlocal voltage.[44,45]

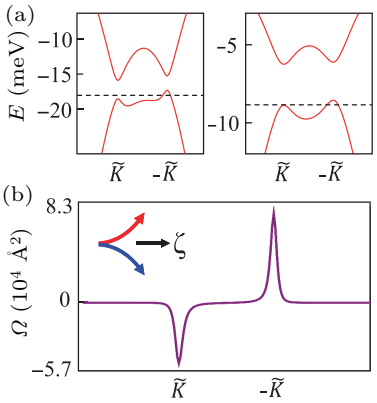


Fig. 4. (a) Two topmost moiré minibands for $L = 27a$ (left) and $L = 42a$ (right). (b) Berry curvature of the topmost band for $L = 27a$. Inset: the asymmetry in the two moiré valleys leads to a spin Hall current contributed from the two original $\pm K$ valleys. ζ denotes an in-plane external electric field. The curved red (blue) arrow denotes spin up (down) Hall current.

3.3. Asymmetric moiré valleys due to triangular wrapping

Because the Berry curvature in the two moiré valleys $\pm\widetilde{K}$ of a long-period moiré described by Eq. (6) has opposite value, there is no net charge Hall current. However, we find that when reducing the moiré periodicity, the moiré valleys in the miniband obtained directly from Eq. (5) become asymmetric, with different alignment and band gap [c.f. Fig. 4(a)]. This is because the two moiré valley states at $\widetilde{K}$ and $-\widetilde{K}$ are located at opposite directions measured from the original K point, which are inequivalent arising from the triangular wrapping effect. This wrapping effect is proportion to k^3, with k being the momentum measured from K point in the original Brillouin zone, and is strong for a short-period moiré pattern with a corresponding large moiré Brillouin zone. Because of this asymmetry in the two Dirac cones, the Berry curvature from the two moiré valleys $\pm\widetilde{K}$ does not have opposite values any more, resulting in a charge Hall current at each original valley [c.f. Fig. 4(b)]. With the increase of moiré period L, the triangular wrapping effect fades out gradually. As a consequence, the Berry curvatures at the two moiré valleys approach opposite values. Considering the strong SOC in the valence band of TMDs, this charge Hall current is spin polarized. In the presence of time-reversal symmetry, there is a net spin Hall current

contributed from the two original $\pm K$ valleys, although the total charge Hall current cancels out. Note that in monolayer TMDs, the Berry curvature is very small because of the large band gap. Moiré Dirac fermions in TMD vdW heterostructure are therefore a potential platform to generate large spin and valley currents.

3.4. Light-induced quantum anomalous Hall effect

Light is a powerful tool to engineer physical property in solid state systems.[46–48] In the following, we discuss the effect of light on the moiré Dirac fermions, focusing on the possible nontrivial global band topology. The light–matter interaction is introduced via the minimal substitution, i.e., $\boldsymbol{k} \to \boldsymbol{k} + e\boldsymbol{A}(t)$ with $\boldsymbol{A}(t)$ being the vector potential of the applied electromagnetic field. For concreteness, we consider a circularly polarized light, which has $\boldsymbol{A}(t) = A_0(\eta\cos\Omega t, \sin\Omega t)$ with $\Omega = 2\pi/T$ being the frequency of light, A_0 being its amplitude, and $\eta = \pm 1$ denoting its chirality. We note that the linearly polarized light is a superposition of the left and right circularly polarized light, $\boldsymbol{A}(t) = A_0(0, \sin\Omega t)$. The light–matter interaction is totally determined by a dimensionless constant $\mathcal{A} = eA_0L/\hbar$. We notice that time-reversal symmetry is broken when a circularly polarized light is applied to the system.

Light driving renders the moiré Dirac Hamiltonian time-periodic, $H_{\rm L}(t) = H_{\rm L}(t+T)$ with periodicity T, which can be solved using the Floquet theory. This theory states that the solution of the Schrödinger equation of a time-periodic Hamiltonian is a product of a phase factor and a time periodic state, i.e., $|\psi(t)\rangle = {\rm e}^{-{\rm i}\varepsilon t}|u(t)\rangle$, where the time periodic function $|u(t)\rangle = |\, u(t+\ \frac{2\pi}{\Omega})\rangle$ is the Floquet state and ε is the quasienergy, satisfying

$$H_{\rm F}^t = \left[H(t) - {\rm i}\hbar\frac{\partial}{\partial t}\right]|u(t)\rangle = \varepsilon|u(t)\rangle, \tag{7}$$

where $H_{\rm F}^t$ is called the Floquet Hamiltonian, which can be diagonalized in the extended space $|\alpha, n\rangle$ consisting of the electronic basis $|\alpha\rangle$ and photonic basis $|n\rangle$.

Because the moiré Dirac gap is on the order of meV, the typical light frequency is far off-resonant for any electron transitions. The influence of an off-resonant light can be captured in an effective static Hamiltonian, i.e., $H_{\rm eff} = \frac{\rm i}{T}\log(U)$, in which $U = \mathcal{T}\exp\left(-{\rm i}\int_0^T H(t){\rm d}t\right)$ is the time evolution operator of the system over one period and $\mathcal{T}$ is the time-ordering operator. In the limit of $\mathcal{A}^2 \ll 1$, it has been shown that $H_{\rm eff}$ has the following form:[49]

$$\begin{aligned} H_{\rm eff} &\approx H_0 + \frac{[H_{-1}, H_1]}{\Omega} + O\left(\mathcal{A}^4\right) \\ &\approx v(\widetilde{\tau}\sigma_x k_x + \sigma_y k_y) + \frac{\Delta}{2}\sigma_z + \eta\widetilde{\tau}\frac{v^2\mathcal{A}^2}{\Omega}\sigma_z, \end{aligned} \tag{8}$$

with H_n being the discrete Fourier component of the Hamiltonian, i.e., $H_n = \frac{1}{T}\int_0^T H(t)\,{\rm e}^{{\rm i}t\Omega n}{\rm d}t$ and $v = \frac{\sqrt{3}}{2}Lt_0$ being the effective velocity of moiré Dirac electrons, k_x and k_y being momenta measured away from the moiré Dirac points, and σ_i being the Pauli matrix acting on the moiré sublattice degree of freedom. Contrary to the staggered potential term (the second term), the light-induced mass term (the third term) has opposite signs for the two valleys. This effective Hamiltonian resembles the one proposed by Haldane with a topologically nontrivial mass $\eta\widetilde{\tau}\frac{v^2\mathcal{A}^2}{\Omega}$ and an additional topologically trivial sublattice potential $\Delta/2$. We note that the mass terms induced by the circularly polarized light have opposite signs for the two original valleys $\pm K$.

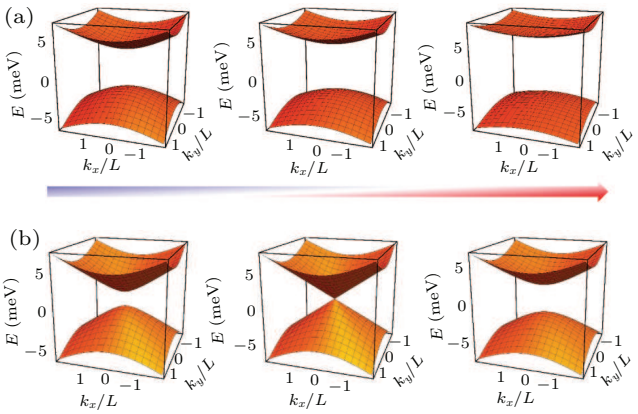


Fig. 5. Evolution of the band structure of an effective static Hamiltonian ($\eta = 1$) at $\widetilde{K}$ (a) and $-\widetilde{K}$ (b) valleys with increasing the light driving strength, $\mathcal{A} = \mathcal{A}_0/\sqrt{2}$ (left), $\mathcal{A} = \mathcal{A}_0$ (middle), $\mathcal{A} = \sqrt{2}\mathcal{A}_0$ (right). Other parameters used are $\Delta = 3.845$ meV, $\Omega = 8.0t_0$, $t_0 = 2.37$ meV.

Figure 5 shows the evolution of energy spectrum with the increase of the strength of the applied light for the two moiré valleys. We find that the circularly polarized light breaks the degeneracy of the two moiré valleys and leads to qualitatively different gap evolution behavior. In particular, the energy gap of $\widetilde{K}$ valley increases monotonically, while the one at $-\widetilde{K}$ valley decreases monotonically first, then closes at the critical value $\mathcal{A} = \mathcal{A}_0 \equiv \sqrt{\Delta\Omega/2}/v$, and finally reopens. The gap evolution behavior at $-\widetilde{K}$ valley reminds us of a topological phase transition. We then calculate the Berry curvature of the two moiré valleys under light driving before and after the topological phase transition [c.f. Figs. 6(b) and 6(c)], and compare them with those without light driving [c.f. Fig. 6(a)]. We find that after driving, the Berry curvatures of the two moiré valleys no longer have time reversal symmetry. In particular, the Berry curvatures of the $\widetilde{K}$ valley before and after the phase transition are both negative, and their magnitudes decrease with the increase of the light driving strength; While for the $-\widetilde{K}$ valley, the Berry curvature changes from positive value to negative one after the phase transition. After integrating the Berry curvature at each valley, we find that the Chern number is changed from 0.5 to -0.5 at $-\widetilde{K}$ valley. In contrast, the calculated Chern number is always -0.5 at $\widetilde{K}$ valley independent of the light strength. In total, the Chern number of the whole moiré system is then changed from 0 to -1 through a light-induced

topological phase transition, which means that the strong light-driving moiré system is in the quantum anomalous Hall phase. When changing the circulation of the polarized light ($\eta = -1$), the energy gap at the $\widetilde{K}$ valley first closes and then reopens, in which the Chern number is changed from -0.5 to 0.5. The total Chern number is then changed from 0 to 1.

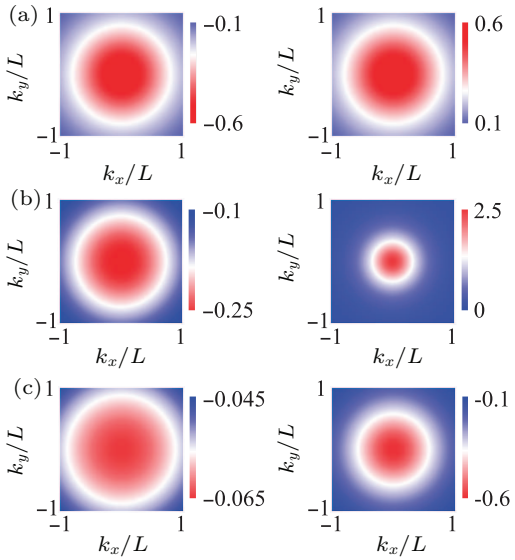


Fig. 6. Distribution of Berry curvature in the conduction band around the $\widetilde{K}$ (left) and $-\widetilde{K}$ (right) valleys. (a) Without light driving. (b) With $\mathcal{A} = \mathcal{A}_0/\sqrt{2}$. (c) With $\mathcal{A} = \sqrt{2}\mathcal{A}_0$. The calculated Chern numbers are $C_c = -0.5$ for $\widetilde{K}$ valley and $C_c = 0.5$ for $-\widetilde{K}$ valley in (a) and (b), and $C_c = -0.5$ for both $\widetilde{K}$ and $-\widetilde{K}$ valleys in (c). The parameters are the same as those in Fig. 5.

To further study the light-induced topological phase in the moiré Dirac system, we construct an effective Haldane model to study the in-gap edge states. The effective TB Hamiltonian reads[50]

$$\mathcal{H} = t_1 \sum_{\langle i,j\rangle} c_i^\dagger c_j + t_2 \sum_{\langle\langle i,j\rangle\rangle} \mathrm{e}^{\pm \mathrm{i}\phi} c_i^\dagger c_j + \sum_i \varepsilon_i c_i^\dagger c_j, \tag{9}$$

where $\langle i,j\rangle$ denotes the nearest-neighbor hopping, and $\langle\langle i,j\rangle\rangle$ denotes the next nearest-neighbor hopping, with t_1 and t_2 being their corresponding hopping strengths. We use the convention that the next nearest-neighbor hoppings in a clockwise direction have an extra $-\phi$ phase while the ones in the counterclockwise direction have $+\phi$ phase [c.f. Fig. 7(a)]. The correspondence between the effective Hamiltonian Eq. (8) and TB Hamiltonian Eq. (9) leads to the following relation: $t_1 = t_0$, $t_2 = \frac{1}{4\sqrt{3}} \frac{t_0^2 \mathcal{A}^2}{\Omega}$, and $\phi = \pi/2$.

Without light driving, the bulk states in a zigzag nanoribbon geometry at the two valleys are symmetric and connected by two trivial flat bands [c.f. Fig. 3(d)]. Upon driving, the two valleys become asymmetric due to the breaking of time reversal symmetry and the bulk gap of the $-\widetilde{K}$ valley closes at the topological phase transition point [c.f. Fig. 7(b)]. Interestingly, when further increasing the light driving strength, the gap reopens and a pair of chiral edge states appear in the bulk gap [c.f. Fig. 7(c)]. These edge states distribute at opposite boundaries and propagate in opposite directions [c.f. Fig. 7(d)].

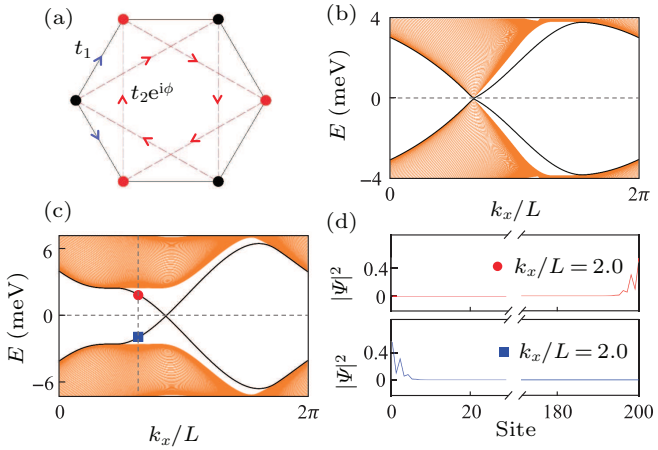


Fig. 7. (a) Schematic of a honeycomb lattice with nearest-neighbor hopping t_1 and next nearest-neighbor hopping t_2 with a phase $\phi = \pi/2$. (b) Energy spectrum of a zigzag nanoribbon with light driving strength $\mathcal{A} = \mathcal{A}_0$. (c) The same as (b) with $\mathcal{A} = \sqrt{2}\mathcal{A}_0$. (d) Distribution of wavefunction of the two in-gap states shown in (c). The parameters are the same as those in Fig. 5.

4. Conclusions

We have revealed moiré Dirac fermions with tunable large Berry curvature in a moiré superlattice of TMD heterobilayer. These novel Dirac fermions are formed by the moiré potential with two nearly degenerate local maxima. By applying on-site potential on the two outmost zigzag edges of the moiré lattice, we can tune the gapped flat-band edge states into the gapless helical ones. In short-period moiré patterns, we find that the two moiré valleys become asymmetric due to the triangular wrapping effect, which produces a net spin Hall current. More interestingly, a circularly polarized light can drive these topologically trivial moiré Dirac fermions into a quantum anomalous Hall phase. Our results open up a new possibility to study the Dirac physics in two dimensions, with potential applications in constructing valleytronic devices in moiré scale.

Acknowledgements

Project supported by the Science Fund for Distinguished Young Scholars of Hunan Province (Grant No. 2022J10002), the National Key Research and Development Program of China (Grant No. 2021YFA1200503), and the Fundamental Research Funds for the Central Universities from China.

References

[1] Rycerz A, Tworzydło J and Beenakker C 2007 *Nat. Phys.* **3** 172
[2] Liu G B, Xiao D, Yao Y, Xu X and Yao W 2015 *Chem. Soc. Rev.* **44** 2643
[3] Xu X, Yao W, Xiao D and Heinz T F 2014 *Nat. Phys.* **10** 343
[4] Schaibley J R, Yu H, Clark G, Rivera P, Ross J S, Seyler K L, Yao W and Xu X 2016 *Nat. Rev. Mater.* **1** 1

[5] Vitale S A, Nezich D, Varghese J O, Kim P, Gedik N, Jarillo-Herrero P, Xiao D and Rothschild M 2018 *Small* **14** 1801483
[6] Xiao D, Chang M C and Niu Q 2010 *Rev. Mod. Phys.* **82** 1959
[7] Xiao D, Yao W and Niu Q 2007 *Phys. Rev. Lett.* **99** 236809
[8] Yao W, Xiao D and Niu Q 2008 *Phys. Rev. B* **77** 235406
[9] Xiao D, Liu G B, Feng W, Xu X and Yao W 2012 *Phys. Rev. Lett.* **108** 196802
[10] Zeng H, Dai J, Yao W, Xiao D and Cui X 2012 *Nat. Nanotechnol.* **7** 490
[11] Mak K F, He K, Shan J and Heinz T F 2012 *Nat. Nanotechnol.* **7** 494
[12] Cao T, Wang G, Han W, *et al*. 2012 *Nat. Commun.* **3** 887
[13] Mak K F, McGill K L, Park J and McEuen P L 2014 *Science* **344** 1489
[14] Yuan H, Wang X, Lian B, *et al*. 2014 *Nat. Nanotechnol.* **9** 851
[15] Zhang Y, Oka T, Suzuki R, Ye J and Iwasa Y 2014 *Science* **344** 725
[16] Geim A K and Grigorieva I V 2013 *Nature* **499** 419
[17] Ponomarenko L, Gorbachev R, Yu G, *et al*. 2013 *Nature* **497** 594
[18] Hunt B, Sanchez-Yamagishi J D, Young A F, *et al*. 2013 *Science* **340** 1427
[19] Gorbachev R, Song J, Yu G, Kretinin A, *et al*. 2014 *Science* **346** 448
[20] Zhang C, Chuu C P, Ren X, Li M Y, Li L J, Jin C, Chou M Y and Shih C K 2017 *Science Advances* **3** e1601459
[21] Tong Q, Yu H, Zhu Q, Wang Y, Xu X and Yao W 2017 *Nat. Phys.* **13** 356
[22] Tong Q, Liu F, Xiao J and Yao W 2018 *Nano Lett.* **18** 7194
[23] Yu H, Liu G B, Tang J, Xu X and Yao W 2017 *Science Advances* **3** e1701696
[24] Wu F, Lovorn T and MacDonald A 2018 *Phys. Rev. B* **97** 035306
[25] Seyler K L, Rivera P, Yu H, Wilson N P, Ray E L, Mandrus D G, Yan J, Yao W and Xu X 2019 *Nature* **567** 66
[26] Tran K, Moody G, Wu F, *et al*. 2019 *Nature* **567** 71
[27] Jin C, Regan E C, Yan A, *et al*. 2019 *Nature* **567** 76
[28] Cao Y, Fatemi V, Fang S, Watanabe K, Taniguchi T, Kaxiras E and Jarillo-Herrero P 2018 *Nature* **556** 43
[29] Stepanov P, Das I, Lu X, Fahimniya A, Watanabe K, Taniguchi T, Koppens F H, Lischner J, Levitov L and Efetov D K 2020 *Nature* **583** 375
[30] Oh M, Nuckolls K P, Wong D, Lee R L, Liu X, Watanabe K, Taniguchi T and Yazdani A 2021 *Nature* **600** 240
[31] Cao Y, Rodan-Legrain D, Park J M, Yuan N F, Watanabe K, Taniguchi T, Fernandes R M, Fu L and Jarillo-Herrero P 2021 *Science* **372** 264
[32] Sharpe A L, Fox E J, Barnard A W, Finney J, Watanabe K, Taniguchi T, Kastner M and Goldhaber-Gordon D 2019 *Science* **365** 605
[33] Serlin M, Tschirhart C, Polshyn H, Zhang Y, Zhu J, Watanabe K, Taniguchi T, Balents L and Young A 2020 *Science* **367** 900
[34] Liu G B, Shan W Y, Yao Y, Yao W and Xiao D 2013 *Phys. Rev. B* **88** 085433
[35] Wu F, Lovorn T, Tutuc E and MacDonald A H 2018 *Phys. Rev. Lett.* **121** 026402
[36] Giannozzi P, Baroni S, Bonini N, *et al*. 2009 *J. Phys.: Condens. Matter* **21** 395502
[37] Giannozzi P, Andreussi O, Brumme T, *et al*. 2017 *J. Phys.: Condens. Matter* **29** 465901
[38] Grimme S, Antony J, Ehrlich S and Krieg H 2010 *The Journal of Chemical Physics* **132** 154104
[39] Tang Y, Li L, Li T, *et al*. 2020 *Nature* **579** 353
[40] Yao W, Yang S A and Niu Q 2009 *Phys. Rev. Lett.* **102** 096801
[41] Dong J W, Chen X D, Zhu H, Wang Y and Zhang X 2017 *Nat. Mater.* **16** 298
[42] Lu J, Qiu C, Ye L, Fan X, Ke M, Zhang F and Liu Z 2017 *Nat. Phys.* **13** 369
[43] Zhang D W, Zhu Y Q, Zhao Y, Yan H and Zhu S L 2018 *Advances in Physics* **67** 253
[44] Sui M, Chen G, Ma L, *et al*. 2015 *Nat. Phys.* **11** 1027
[45] Shimazaki Y, Yamamoto M, Borzenets I V, Watanabe K, Taniguchi T and Tarucha S 2015 *Nat. Phys.* **11** 1032
[46] Rudner M S and Lindner N H 2020 *Nat. Rev. Phys.* **2** 229
[47] Bao C, Tang P, Sun D and Zhou S 2022 *Nat. Rev. Phys.* **4** 33
[48] Zhan F, Ning Z, Gan L Y, Zheng B, Fan J and Wang R 2022 *Phys. Rev. B* **105** L081115
[49] Kitagawa T, Oka T, Brataas A, Fu L and Demler E 2011 *Phys. Rev. B* **84** 235108
[50] Haldane F D M 1988 *Phys. Rev. Lett.* **61** 2015